Rodríguez-Martínez, J.A.; Vadillo, G.; Rittel, D.; Zaera, R.; Fernández-Sáez, J. (2015). Dynamic recrystallization and adiabatic shear localization. *Mechanics of Materials*, vol. 81, pp. 41-55.

DOI: https doi.org 10.101 .mechmat.2014.10.001

Dynamic recrystallization and adiabatic shear localization

J. A. Rodríguez-Martínez[a,b,*], G. Vadillo[a], D. Rittel[b], R. Zaera[a], J. Fernández-Sáez[a]

[a] *Department of Continuum Mechanics and Structural Analysis. University Carlos III of Madrid. Avda. de la Universidad, 30. 28911 Leganés, Madrid, Spain*
[b] *Faculty of Mechanical Engineering, Technion. 32000 Haifa, Israel*

Abstract

It has recently been reported that, in alloys exhibiting early dynamic recrystallization (DRX), the onset of adiabatic shear bands (ASB) is primarily related to microstructural transformations, instead of the commonly assumed thermal softening mechanism as shown by Rittel et al. (2006, 2008) and Osovski et al. (2012b). Further, the dominant role of microstructural softening in the necking process of dynamically stretching rods showing DRX has been verified using linear stability analysis and finite element simulations by Rodríguez-Martínez et al. (2014). With the aim of extending this coupled methodology to shear conditions, this paper presents an analytical solution to the related problem of ASB in a material that undergoes both twinning and dynamic recrystallization. A special prescription of the initial and loading conditions precludes wave propagation in the specimen which retains nevertheless its inertia, allowing for a clear separation of material versus structural effects on the localization process. A parametric study, performed on the constants of the constitutive model, permits the identification of their relative role in the onset of the dynamic instability. The main outcome of the analysis confirms the strong destabilizing effect played by the development of DRX, consistently with the former statement regarding ASB, and contributes to rationalize the observations of other authors.

Keywords:
Adiabatic shear band, Linear stability analysis, Numerical simulation, Dynamic recrystallization, Thermal softening

*Corresponding author. Tel. +34916248460; Fax: +34916249430. e-mail: jarmarti@ing.uc3m.es

1. Introduction

The analysis of dynamic shear instabilities, such as adiabatic shear bands (ASB), is of capital importance for the understanding of ductile failure of metals at high rates of deformation. The interested reader can find a wealth of experimental evidence in Bai and Dodd's book (Bai and Dodd, 2012), and a summary of the analytical results in Wright's book (Wright, 2002). The development of adiabatic shear bands is assumed to occur in three different stages: in the first step, the strain is homogeneous, and the strain hardening of the material overcomes any kind of heterogeneity present in the material; in the second step, after the maximum stress has been reached, a diffuse instability starts to develop due to the presence of softening effects. The strain begins to be rather heterogeneous. In the third stage, a strong instability is formed and deformation localizes in a narrow band (Marchand and Duffy, 1998). For decades, the classical explanation of Zener and Hollomon (1944) has been the prevailing assumption, which consists of the competition between strain hardening and thermal softening. Accordingly, adiabatic shear bands generation, as a typical mechanical instability, has been extensively studied by many authors. This instability can be triggered by both geometrical imperfections and the mechanical softening due to heat generation (thermal softening). However, the recent work by Osovski et al. (2012b) has challenged this assumption of a unique softening mechanism. These authors showed experimentally that, in addition to the potential effect of thermal softening, microstructural evolutions, such as dynamic recrystallization DRX, may indeed cause local softening and shear localization. Using a sort of "coarse-grained" finite element model, these authors assessed the relative influence that microstructural changes, and thermal softening may have on the shear band formation (Osovski et al., 2013). One of their main results was that, even in the absence of noticeable thermal softening, microstructural softening can be in itself a potent destabilizing mechanism.

Among the several analytical solutions for the dynamic shear localization problem, the seminal work of Molinari and Clifton (1987) is among the first to propose a structured approach to predict the onset and initial evolution of the instabilities. One should also mention here the work of Rodríguez-Martínez et al. (2014) who analyzed the onset of dynamic tensile necking using a perturbation analysis, for a material that can undergo both

thermal and microstructural softening. It is therefore interesting to re-analyze dynamic shear localization, in the spirit of the above-mentioned authors, with the support of both analytical and numerical simulations, to broaden the problem and its solution to the general case of dynamic instabilities, thereby complementing the results for dynamic necking.

Therefore, the essence of this paper is an assessment of the onset of dynamic shear instabilities, using the approach of Molinari and Clifton (1987) and Molinari (1997), with an additional microstructural softening mechanism in accordance with the results of Osovski et al. (2012b). The idea is to generalize our approach proposed for the dynamic necking problem by adding the dynamic shear localization analysis. Consequently, we consider here a rectangular 2D plane-strain solid, treated analytically as a 1D solid, subjected to dynamic shear. The material can undergo both thermal and microstructural softening. From the modeling point of view, and following Molinari and Clifton (1987) and Molinari (1997), shear localization can be derived as the evolution of an initial perturbation. This problem is addressed within a 1D linear stability analysis, where the uncontrolled growth of the perturbation signals the onset of the shear instability. Next, the same problem is modelled numerically by considering a layer of finite thickness subjected to constant velocities at the boundaries, enforcing a shear loading configuration. Note that the problem is formulated in a way that cancels wave propagation effects (Rodríguez-Martínez et al., 2014; Zaera et al., 2014), such as to emphasize purely material aspects of the problem.

The main outcome of the analysis confirms the strong destabilizing effect played by the development of DRX in addition to thermal softening, in full accord with previous experimental evidence. In that respect, the present analysis complements and adds more generality to the problem of dynamic mechanical instabilities in strained solids.

The paper is organized as follows: the second section introduces briefly the 1D constitutive model for the material considered (Ti6Al4V). The third and fourth sections are devoted to present the linear stability methodology and the finite element modelling of the dynamic simple shear problem, respectively, taking into account strain-rate sensitivity and thermal effects, as well as microstructural transformations (twinning and DRX). The salient features of the stability analysis and the main results obtained from it are presented in sections 5 and 6 respectively, while in section 7 the results from the FEM analysis are

summarized. Sections 8 includes a brief discussion of the results and the final conclusions are given in section 9.

2. 1D constitutive model for Ti6Al4V alloy

The material is assumed to obey Huber-Mises plasticity. The model considers three possible mechanisms responsible for the plastic flow: Slip, twinning and dynamic recrystallization (DRX). Those three mechanisms are treated using a rule of mixture to describe the mechanical behaviour of the material. In the undeformed configuration the material is free of twins and DRX. Twinning is triggered by plastic deformation and complements dislocation activity, thereby increasing the flow stress and strain hardening. Twinning is assumed to stop once DRX starts, whose onset is determined by a threshold value of the stored energy of cold work (Osovski et al., 2013). Dynamic recrystallization contributes to the material strain softening. Strain rate and temperature sensitivities of the flow stress are included in the material description. For the sake of brevity, only the main features of the model are presented in this paper while further details can be found in Osovski et al. (2013).

The thermo-viscoplastic flow law has the general form:

$$\tau_y = \Psi\left(\gamma^p, \dot{\gamma}^p, T\right) = h\left(\gamma^p\right) s\left(\dot{\gamma}^p\right) p\left(T\right) \tag{1}$$

where the functions $h\left(\gamma^p\right)$, $s\left(\dot{\gamma}^p\right)$ and $p\left(T\right)$ define the plastic strain γ^p, plastic strain rate $\dot{\gamma}^p$ and temperature T dependencies of the material.

- The function $h\left(\gamma^p\right)$ is composed by three terms and reads as follows:

$$h\left(\gamma^p\right) = \left(1 - f_{DRX}\right)\tau_y^0 + f_{DRX}\tau_y^{DRX} + \left(1 - f_{DRX} - f_{twins}\right)\left(\tau_t\left(\frac{1}{\chi}\right) + \tau_d\left(\gamma^p\right)^n\right) \tag{2}$$

  where f_{DRX} and f_{twins} are the volume fractions of DRX and twins respectively. The first yield stress term in the previous expression represents the initial yield stress of the material –which is controlled by the slip phase– and it is defined by τ_y^0. The

second yield stress term is to be understood as the flow stress at which DRX first appears (upon reaching the energetic threshold given by U_{DRX}, see Eqs. (3)-(4)). This is determined by the parameter $\tau_y^{DRX} = \tau_y|_{U=U_{DRX}}$ that has to be calculated in the integration procedure for each loading case. The third yield stress term is an isotropic strain hardening function where τ_t, τ_d and n are material constants and χ is given by $\chi = \frac{2\zeta(1-f_{twins})}{f_{twins}}$ with ζ being a material parameter.

The evolution law for the twins volume fraction is as follows:

$$f_{twins} = g\left(\gamma^p\right) = \begin{cases} \frac{1}{N}\left[\arctan\left(2\pi a\gamma^p - 2\pi d\right) - \arctan\left(-2\pi d\right)\right]; & U < U_{DRX} \\ f^*_{twins} = f_{twins}|_{U=U_{DRX}}; & U \geqslant U_{DRX} \end{cases} \tag{3}$$

where U is the stored energy of cold work (see Eq. (5)) and U_{DRX} is the threshold energy for the onset of the recrystallization process. Here, a, d and N are material constants which describe the volume fraction of twins upon plastic strain.

The evolution law for the DRX volume fraction is defined by:

$$f_{DRX} = w\left(U\right) = \begin{cases} 0; & U < U_{DRX} \\ 1 - \exp\left(-k_{DRX}\left(\frac{U-U_{DRX}}{U_{DRX}}\right)^{n_{DRX}}\right); & U \geqslant U_{DRX} \end{cases} \tag{4}$$

where k_{DRX} and n_{DRX} are material parameters which describe the volume fraction of DRX upon plastic strain.

The stored energy is calculated by:

$$U = \left(1 - f_{DRX} - f_{twins}\right)\left(1 - \beta\right)\int_0^{\gamma^p} \tau d\gamma^p \tag{5}$$

where β is the Taylor-Quinney coefficient of the phase undergoing slip which is assumed as constant.

- The function $s\left(\dot{\gamma}^p\right)$ reads as follows:

$$s\left(\dot{\gamma}^p\right) = \left(\frac{\dot{\gamma}^p}{\dot{\gamma}_{ref}}\right)^m \tag{6}$$

where $\dot{\gamma}_{ref}$ is the reference strain rate and m is the strain rate sensitivity parameter.

- The function $p\left(T\right)$ reads as follows:

$$p\left(T\right) = \left(1 - \alpha\Delta T\right) \tag{7}$$

where α is the temperature sensitivity parameter and $\Delta T = T - T_0$, being T the current temperature and T_0 the initial temperature.

The yield condition may be written as

$$\Phi = \bar{\sigma} - \sqrt{3}\Psi\left(\gamma^p, \dot{\gamma}^p, T\right) = 0 \tag{8}$$

where $\bar{\sigma}$ is the Huber-Mises equivalent stress.

The values of the material parameters corresponding to Ti6Al4V alloy are given in Table 1.

Despite the simple formulation of this constitutive model, we claim that it allows to explore the respective roles played by DRX and thermal softening on the inception of shear bands, as further discussed in sections 6 and 7. Note that previous 1D constitutive model can be extended to a 3D framework as described in Rodríguez-Martínez et al. (2014).

3. Problem formulation and linear stability analysis

3.1. Governing equations

The problem addressed is based on the configuration reported by Molinari (1997). The problem is modelled as that of a layer infinitely extended in the shear direction x and in the out-of-plane direction z, with finite thickness $2b$ in the direction y (see Fig. 1). At the upper and lower surfaces, constant velocities $\pm v_0$ are applied, parallel to the x direction. It

Symbol	Property and units	Value
τ_y^0	Initial shear yield stress (MPa), Eq. (2)	288.67
τ_t	Strain hardening parameter ($mMPa$), Eq. (2)	1.039×10^{-3}
ζ	Average twin width (μm), Eq. (2)	2
τ_d	Strain hardening parameter (MPa), Eq. (2)	124.130
n	Strain hardening exponent, Eq. (2)	0.25
$\dot{\gamma}_{ref}$	Reference strain rate (s^{-1}), Eq. (6)	10^3
T_0	Initial temperature (K), Eq. (7)	293
N	Material parameter, Eq. (3)	7.4594
a	Material parameter, Eq. (3)	5
d	Material parameter, Eq. (3)	1
k_{DRX}	Material parameter, Eq. (4)	0.5
n_{DRX}	Material parameter, Eq. (4)	8.7
m^*	Reference strain rate sensitivity exponent	0.00539
α^*	Reference temperature sensitivity parameter (K^{-1})	10^{-4}
U^*	Reference threshold energy for DRX formation (MJ/m^3)	92
G	Elastic shear modulus (GPa)	43.6
K	Elastic bulk modulus (GPa)	116
β	Taylor-Quinney coefficient, Eqs. (5) and (14)	0.6
k	Thermal conductivity (W/mK), Eq. (14)	21.9
l_h	Transformation latent heat (MJ/m^3), Eq.(14)	118
ρ	Density (kg/m^3), Eq. (9)	4500
c	Specific heat (MJ/m^3K), Eq. (14)	234

Table 1: *Parameters related to shear yield stress, DRX and twins volume fractions, stiffness parameters, and conventional material constants representative of titanium alloys. The values are taken from Rodríguez-Martínez et al. (2014) and adapted here to the shear configuration.*

is supposed that this loading condition is always satisfied, and therefore elastic unloading is disregarded. The layer material is taken to be incompressible, of mass density ρ, with a constitutive behaviour described by Eqs. (1-8).

The problem is formulated in a one-dimensional framework, the variables depending solely upon the coordinate y and the time t. The velocity of a particle is parallel to the shear direction x and is denoted by v. To be noted that the problem can be formulated, indistinctly, in Eulerian or Lagrangian coordinates since both descriptions are coincident for the specific configuration addressed.

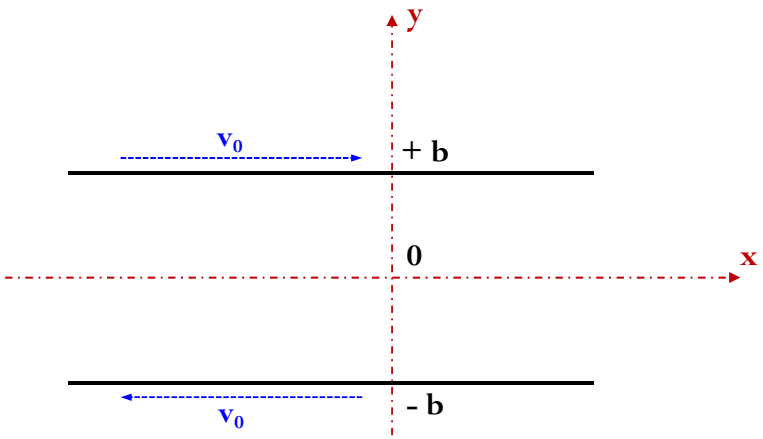

Figure 1: Schematic representation of the geometry and loading conditions of the problem addressed. Adapted from Molinari (1997).

Since large deformations are considered, elasticity can be neglected and $\gamma^p = \gamma$ The fundamental equations governing the loading process are presented below:

- Momentum balance:

$$\rho \frac{\partial v}{\partial t} = \frac{\partial \tau}{\partial y} \tag{9}$$

- Compatibility condition:

$$\dot{\gamma} = \frac{\partial v}{\partial y} \tag{10}$$

- Flow stress:

$$\tau_y = \Psi\left(\gamma, \dot{\gamma}, T\right) \tag{11}$$

where the strain γ is defined by

$$\gamma(t) = \int_0^t |\dot{\gamma}(\varsigma)| d\varsigma$$

- Twinning transformation law: from Eq. (3)

$$f_{twins} = g\left(\gamma\right) \tag{12}$$

- DRX transformation law: from Eq. (4)

$$f_{DRX} = w\left(U\right) \tag{13}$$

- Conservation of energy: assuming no heat flow at the specimen's boundaries and neglecting the contribution of thermoelastic effects:

$$c\frac{\partial T}{\partial t} = \beta\tau\dot{\gamma} + k\frac{\partial^2 T}{\partial y^2} + \frac{\partial f_{DRX}}{\partial t} l_h \tag{14}$$

where c, k and l_h stand for the heat capacity per unit volume, the thermal conductivity and the latent heat per unit volume of transformed DRX due to the exothermic character of the phase transformation (Zaera et al., 2013).

Considering the domain $[-b, b]$, the equations (9-14) are to be solved under the following initial conditions:

$$
\begin{aligned}
v(y,0) &= \dot{\gamma}_0 y \\
\sigma(y,0) &= \Psi\left(0\right) = \tau_y^0 \\
\gamma(y,0) &= 0 \\
T(y,0) &= T_0 \\
f_{twins}(y,0) &= 0 \\
f_{DRX}(y,0) &= 0
\end{aligned}
\tag{15}
$$

and boundary conditions:

$$
\begin{aligned}
v(b,t) &= -v(-b,t) = \dot{\gamma}_0 b \\
\partial T(y,t)/\partial y|_{y\pm b} &= 0
\end{aligned}
\tag{16}
$$

where $\dot{\gamma}_0 \equiv \dot{\gamma}$ is constant and defines the value of the strain rate in the sample.

3.2. Linear perturbation analysis

Let $\mathbb{S}(y,t) = \left(v(y), \tau(t), \gamma(t), T(t), f_{twins}(t), f_{DRX}(t)\right)^T$ be the fundamental time-dependent solution, at time t, of the previous problem. $\mathbb{S}$ is obtained by integration of Eqs. (9-14) satisfying the initial and boundary conditions previously listed.

At time $t = t_1$, at which the fundamental solution reaches the value $\mathbb{S}_1(y,t_1) = \left(v_1(y), \tau_1, \gamma_1, T_1, f_{twins1}, f_{DRX1}\right)^T$, consider a small perturbation of this solution $\delta\mathbb{S}(y,t)_{t_1}$, with $|\delta\mathbb{S}(y,t)_{t_1}| \ll |\mathbb{S}_1(y,t_1)|$, given by

$$
\delta\mathbb{S}(y,t)_{t_1} = \delta\mathbb{S}_1 e^{i\xi y} e^{\eta(t-t_1)} \tag{17}
$$

where $\delta\mathbb{S}_1 = \left(\delta v, \delta\tau, \delta\gamma, \delta T, \delta f_{twins}, \delta f_{DRX}\right)^T$ is the perturbation amplitude, ξ the wavenumber and η the growth rate of the perturbation at time t_1. The perturbation becomes unstable when $Re(\eta) > 0$. According to Rodríguez-Martínez et al. (2013) the perturbation growth rate η^+ is assumed to represent the onset of localization, the very first stages at which the local plastic flow deviates from the background value.

By substituting Eq. (17) into Eqs. (9-14) and retaining only first-order terms, the following linearized equations are obtained:

- Momentum balance:

$$\rho\eta\delta v - i\xi\delta\tau = 0 \tag{18}$$

- Compatibility condition:

$$i\xi\delta v - \eta\delta\gamma = 0 \tag{19}$$

Concerning the value of the stored energy of cold work, there are two possible scenarios, depending on the perturbation time:

1. The perturbation time t_1 is such that $U < U_{DRX}$

   - Flow stress:

$$\delta\tau - (H + S\eta)\delta\gamma - P\delta T - R\delta f_{twins} = 0 \tag{20}$$

   - Twinning transformation law:

$$\delta f_{twins} - G\delta\gamma = 0 \tag{21}$$

   - DRX transformation law:

$$\delta f_{DRX} = 0 \tag{22}$$

   - Conservation of energy:

$$(c\eta + k\xi^2)\delta T - \beta\dot{\gamma}_1\delta\tau - \beta\tau_1\eta\delta\gamma = 0 \tag{23}$$

2. The perturbation time t_1 is such that $U \geqslant U_{DRX}$

   - Flow stress:

$$\delta\tau - (H + S\eta)\delta\gamma - P\delta T - Q\delta f_{DRX} = 0 \tag{24}$$

   - Twinning transformation law:

$$\delta f_{twins} = 0 \tag{25}$$

   - DRX transformation law:

$$\delta f_{DRX} - W\delta U = 0 \tag{26}$$

     where δU is obtained linearising Eq. (5) as follows

$$\delta U = -(1-\beta)E_s\delta f_{DRX} + (1 - f_{DRX1} - f_{twins1})\,(1-\beta)\tau_1\delta\gamma \tag{27}$$

   - Conservation of energy:

$$(c\eta + k\xi^2)\delta T - \beta\dot{\gamma}_1\delta\tau - \beta\tau_1\eta\delta\gamma + l_h\eta\delta f_{DRX} = 0 \tag{28}$$

In Eqs. (18-28) the following definitions have been used

$$H = \left.\frac{\partial\Psi}{\partial\gamma}\right|_{t_1}; \quad P = \left.\frac{\partial\Psi}{\partial T}\right|_{t_1}; \quad S = \left.\frac{\partial\Psi}{\partial\dot{\gamma}}\right|_{t_1}; \quad Q = \left.\frac{\partial\Psi}{\partial w}\right|_{t_1}; \quad R = \left.\frac{\partial\Psi}{\partial g}\right|_{t_1}$$

$$G = \left.\frac{\partial g}{\partial\gamma}\right|_{t_1}; \quad W = \left.\frac{\partial w}{\partial U}\right|_{t_1}; \quad E_s = \int_0^{\gamma_1}\tau d\gamma$$

A non-trivial solution for $\delta\mathbb{S}_1$ is obtained only if the determinant of the systems of linear algebraic equations (18-23) or (18-19) and (24-28) is equal to zero. Using the following dimensionless variables and constants

$$\bar{\eta} = \frac{\eta}{\dot{\gamma}_1} \; ; \quad \bar{\xi} = b\xi \; ; \quad \psi(\gamma, T) = \frac{\Psi(\gamma, T)}{\tau_y^0}$$

$$\bar{I} = \sqrt{\frac{\tau_y^0}{\rho b^2 \dot{\gamma}_1^2}} \; ; \quad \psi_1 = \frac{\tau_1(t_1)}{\tau_y^0} \; ; \quad \bar{l}_h = l_h \frac{1}{\tau_y^0}$$

$$\tilde{H} = H\frac{1}{\tau_y^0} \; ; \quad \tilde{P} = P\frac{T_0}{\tau_y^0}$$

$$\tilde{Q} = Q\frac{1}{\tau_y^0} \; ; \quad \tilde{R} = R\frac{1}{\tau_y^0} \; ; \quad \tilde{G} = G \; ; \quad \tilde{W} = W\frac{(1 - f_{DRX1} - f_{twins1})\,(1-\beta)\,\tau_1}{W\,(1-\beta)\,E_s + 1}$$

$$\tilde{c} = c\frac{T_0}{\tau_y^0} \; ; \quad \tilde{k} = k\frac{T_0}{\tau_y^0 \dot{\gamma}_1 b^2}$$

The resulting condition is found to be a cubic equation in $\bar{\eta}$

$$B_3\bar{\eta}^3 + B_2\bar{\eta}^2 + B_1\bar{\eta} + B_0 = 0 \tag{29}$$

where the coefficients B_i are given by the following expressions:

$$B_3 = \tilde{c} \tag{30}$$

$$B_2 = -\tilde{P}\beta + \tilde{k}\bar{\xi}^2 + \tilde{c}\tilde{S}\bar{I}^2\bar{\xi}^2 \tag{31}$$

with B_1 and B_0 depending on the perturbation time, namely:

1. The perturbation time t_1 is such that $U < U_{DRX}$

$$B_1 = \bar{I}^2\bar{\xi}^2(\tilde{k}\tilde{S}\bar{\xi}^2 + \tilde{c}\tilde{H} + \tilde{c}\tilde{G}\tilde{R} + \beta\tilde{P}\psi_1) \tag{32}$$

$$B_0 = \tilde{k}\bar{I}^2\bar{\xi}^4(\tilde{H} + \tilde{G}\tilde{R}) \tag{33}$$

2. The perturbation time t_1 is such that $U \geqslant U_{DRX}$

$$B_1 = \bar{I}^2\bar{\xi}^2(\tilde{k}\tilde{S}\bar{\xi}^2 + \tilde{c}\tilde{H} + \tilde{c}\tilde{G}\tilde{Q} + \beta\tilde{P}\psi_1 - \tilde{W}\bar{l}_h\tilde{P}) \tag{34}$$

$$B_0 = \tilde{k}\bar{I}^2\bar{\xi}^4(\tilde{H} + \tilde{W}\tilde{Q}) \tag{35}$$

Eq. (29) gives, for a certain value of the time at perturbation t_1, the real value of $\bar{\eta}$ as a function of the dimensionless wavenumber $\bar{\xi}$. It has to be recalled that the requisite for unstable growth of $\delta\mathbb{S}_1$ is given by the condition $Re\,(\bar{\eta}) > 0$. Eq. (29) has three roots in $\bar{\eta}$, one real and two complex conjugates. Only the one having the greater positive real part has to be considered for the analysis of the dimensionless perturbation growth rate $\bar{\eta}^+$. Moreover, imposing the condition for maximum perturbation growth $\partial\bar{\eta}^+/\partial\bar{\xi} = 0$, the critical wavenumber $\bar{\xi}_c$ and the critical perturbation growth $\bar{\eta}_c^+$ are determined numerically.

It is important to note here that the stability analysis does not allow for calculation of the strain for which the shear band initiates (critical shear strain). However, it allows identifying the dependence of the critical shear strain with material behaviour. Based on previous works of the authors (Vadillo et al., 2012; Rodríguez-Martínez et al., 2013; Zaera et al., 2014), we claim that the critical shear strain correlates with the critical perturbation growth as it will be further shown in this paper.

4. Finite element modelling of dynamic simple shear

This section describes the features of the finite element model developed to simulate dynamic simple shear. The numerical analyses are carried out using the commercial finite

element code ABAQUS/Explicit (Simulia, 2012). Accordingly to the stability analysis, the problem consists of a $2b$ wide layer extended in shear direction x (see Fig. 2). Plane strain is assumed. Due to the skew-symmetry of the problem with respect to the x-axis, only the $y \geqslant 0$ half of the specimen is analysed (see Fig. 2). The prescribed boundary conditions can be formulated as $v_x(x, b, t) = -\dot{\gamma} b$, $v_x(x, 0, t) = 0$ and $v_y(x, 0, t) = v_y(x, b, t) = 0$. In order to avoid the propagation of waves along the layer, caused by the application of these boundary conditions in a solid initially at rest, specific initial conditions consistent with the boundary conditions are imposed (see Zaera et al. (2014) for detailed explanation of these initial conditions).

$$v_x(x, y, 0) = -\dot{\gamma} y \tag{36}$$

Likewise, in order to avoid the abrupt jump in the stress field caused by application of the boundary conditions, the material flow has been initialized in the whole domain with a value of τ equal to the initial yield stress of the material. If neither the velocity nor the stress field were initialized, for sufficiently high velocities the generated wave could induce by itself plastic localization (Needleman, 1991; Xue et al., 2008). Regarding initial thermal conditions, T_0 is set to 293 K in all cases. As in Molinari and Clifton (1987), the shear band formation is triggered (driven) in the finite element simulations by introducing a sinusoidal spatial imperfection. To that aim, a rectangular domain $0 \leq X \leq L_A$, $0 \leq Y \leq b$ is mapped into that defining the undeformed mesh, according to the expressions

$$\begin{aligned} x &= X - \frac{L_A - L_B}{4}\left(\cos\left(\pi\frac{Y}{b}\right) + 1\right)\left(\frac{2X}{L_A} - 1\right) \\ y &= Y \end{aligned} \tag{37}$$

The ratio L_A/L_B defines the amplitude of the imperfection, to which we will refer as Δ (%), Fig. 2. Dimensions of the finite element model are based on the (typical) slot of the Shear-Compression Specimen (SCS) (Vural et al., 2011). The SCS specimen, originally developed by Rittel et al. (2002a,b), was specifically devised to attain large strains within a wide range of strain rates and it has been shown particularly suitable

for the investigation of dynamic shear localization in different ductile materials (Dorogoy and Rittel, 2005, 2006). We take $L_A = 11.94\ mm$, $b = 0.508\ mm$ and $\Delta = 2\ \%$ unless otherwise noted. The latter will be taken as the reference imperfection amplitude and, from this point on, will be denoted by Δ^*. The effect of the imperfection amplitude in the shear band formation is detailed in Appendix A. The bar is meshed using a total of 9400 four-node thermally coupled plain strain reduced integration elements (CPE4RT in ABAQUS notation), 470 elements in the x direction and 20 elements along the y direction. According to the considerations reported by Zukas and Scheffer (2000), the aspect ratio of the elements was kept close to 1:1 ($\sim 0.0254 \times 0.0254\ mm^2$). A mesh convergence study was performed, and the time evolution of different critical output variables, namely stress, strain and shear band inception, were compared against a measure of mesh density until the results converged satisfactorily (details are given in Appendix A).

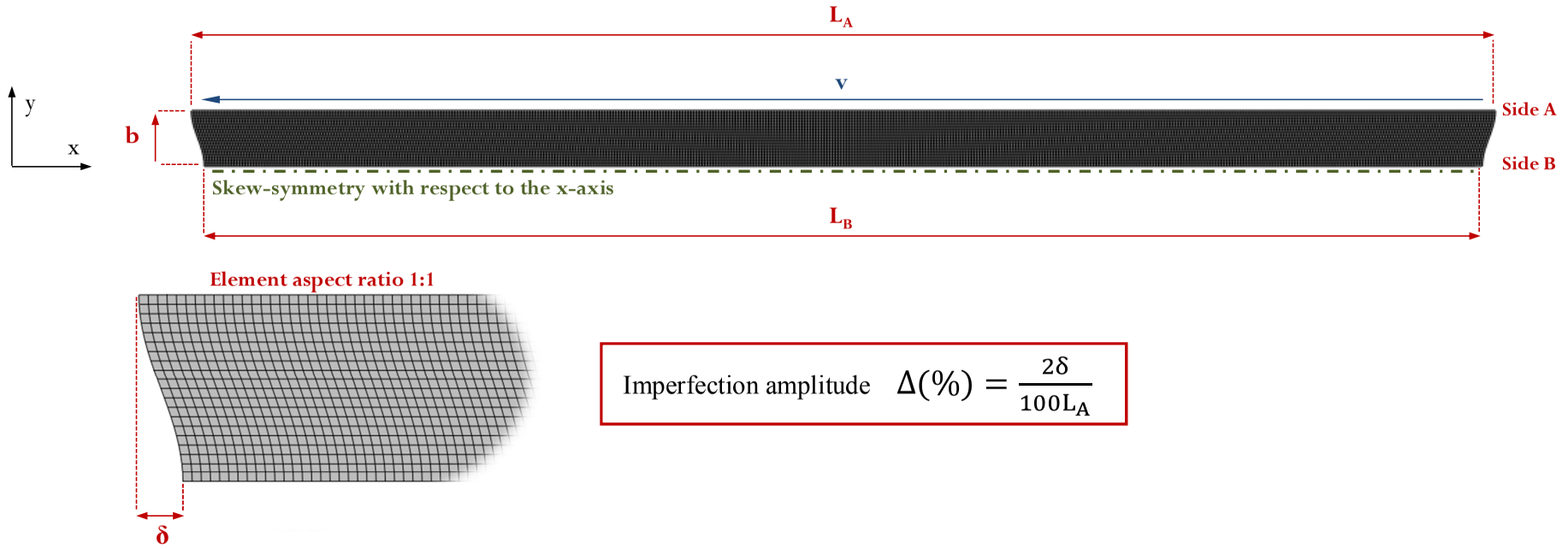

Figure 2: Finite element mesh and mechanical boundary conditions of the simple shear plane strain model.

The set of constitutive equations describing the material behaviour presented in section 2 are implemented in the finite element code through a user subroutine following the integration scheme developed by Zaera and Fernández-Sáez (2006).

5. Salient features of the stability analysis

In this section the main features of the stability analysis are presented and discussed. Unless otherwise noted the material parameters are taken from Table 1. Fig. 3(a) shows the effect of selected material parameters in the curve $\bar{\eta}^+ - \bar{\xi}$. The loading rate is $\dot{\gamma} = 10000\ s^{-1}$. This will be considered as the reference loading rate in all the analyses, and it will be denoted by $\dot{\gamma}^*$. This value lies within the range of strain rates attained in dynamic shear tests devised to analyse shear localization (Klepaczko, 2005). In Fig. 3(a) the results obtained using the reference configuration (parameters listed in Table. 1) are compared with those calculated by setting, alternatively, $m = 0$, $\alpha = 0$ and $k = 0$. We observe that for the reference configuration the curve shows a maximum which determines the critical perturbation growth rate $\bar{\eta}_c^+$ and the dominant wavenumber $\bar{\xi}_c$. As pointed out by Molinari (1997), the existence of a dominant mode results from the competition of different stabilizing effects. Inertia damps the growth of long wavelength modes, while thermal effects and viscosity restrains the growth of small wavelength modes. If $m = 0$, the perturbation growth rate monotonically (and rapidly) increases with $\bar{\xi}$. If $\alpha = 0$ or $k = 0$ the grow rate of the perturbation reaches a horizontal asymptote with increasing $\bar{\xi}$. Following Zaera et al. (2014) and Rodríguez-Martínez et al. (2014), throughout this work we will systematically consider $\bar{\eta}_c^+$ as an indicator of the material stability. The greater the critical perturbation growth, the more unstable the material is. Therefore, the greater the critical perturbation growth, the smaller the strain corresponding to shear localization shall be. This procedure will allow to asses the influence that selected loading and material parameters have in the formation of shear bands. By the same token, the dominant wavenumber allows to determine the characteristic distance between sites where shear localization occurs in problems where multiple shear bands are nucleated (Nesterenko et al., 1989; Nesterenko and Bondar, 1994; Lovinger et al., 2011). Nevertheless, in this paper we will not consider formation of multiple shear bands and the reader is referred to the

seminal paper by Molinari (1997) where an extensive analysis on the collective behaviour and spacing of shear bands is developed.

In Fig. 3(b) the effect of the strain at perturbation γ_1 (strain corresponding to the time at perturbation t_1) in the curve $\bar{\eta}^+ - \bar{\xi}$ is shown. We take $\dot{\gamma} = \dot{\gamma}^*$ and $U_{DRX} = U^*$. Similarly to Molinari (1997), we show that the critical value $\bar{\eta}_c^+$ first increases with γ_1, finds a maximum and then decreases for larger values of the strain at perturbation. It must be noted that this behaviour is specific of dynamic shearing. For instance, if dynamic tensile loading of bars is considered we observe that the critical perturbation growth is an increasing function of the strain at perturbation (Zaera et al., 2014; Rodríguez-Martínez et al., 2014). This analysis on the interplay between $\bar{\eta}_c^+$ and γ_1 could be also conducted in terms of $\bar{\xi}_c$ and γ_1, for which the reader is again referred to Molinari (1997).

6. Stability analysis results

In this section we present the results obtained from the stability analysis. Namely, we systematically investigate the influence of strain rate (section 6.1), strain rate sensitivity (section 6.2), thermal softening (section 6.3) and dynamic recrystallization (section 6.4) in shear localization. Unless otherwise noted, the reference material parameters listed in Table 1 are taken.

6.1. Influence of strain rate

Fig. 4 shows the critical perturbation growth rate $\bar{\eta}_c^+$ versus the strain at perturbation γ_1 for different loading rates: $\dot{\gamma} = 0.01\dot{\gamma}^*$, $\dot{\gamma} = 0.1\dot{\gamma}^*$ and $\dot{\gamma} = \dot{\gamma}^*$. The curve $\bar{\eta}_c^+ - \gamma_1$ hardly depends on the strain rate. The loss of stability of the material starts at $\gamma_1 \approx 1.4$. Larger values of γ_1 lead to increasing $\bar{\eta}_c^+$ up to a maximum in the curve $\bar{\eta}_c^+ - \gamma_1$ is attained (as discussed in Fig. 3) for $\gamma_1 \approx 1.9$. Larger values of γ_1 lead to a *slow* decrease of $\bar{\eta}_c^+$. There is just a small influence of the strain rate in the curve $\bar{\eta}_c^+ - \gamma_1$. As the strain rate decreases the loss of material stability is slightly delayed and the maximum critical perturbation growth is slightly increased. However, these differences are, for all purposes, negligible. Therefore, the stability analysis predicts no influence of the loading rate on the critical perturbation growth. This suggests that, for this specific material behaviour, the loading rate may have

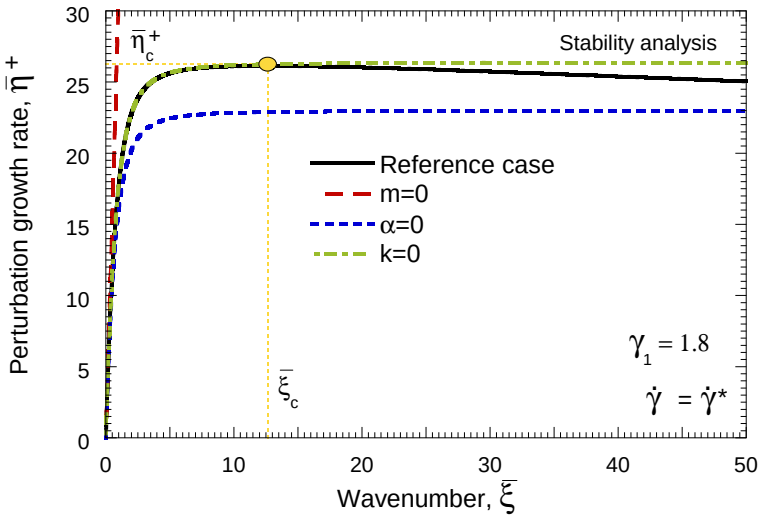

(a)

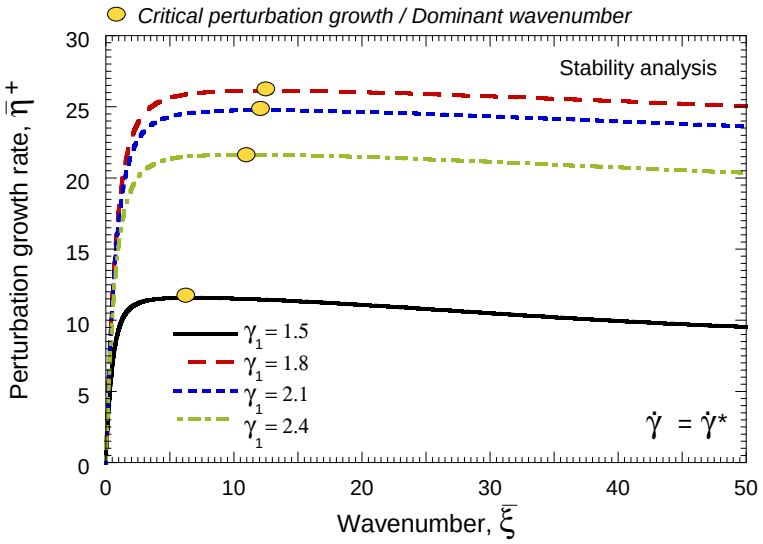

(b)

Figure 3: Stability analysis results. Perturbation growth rate $\bar{\eta}^+$ versus wavenumber $\bar{\xi}$ for $\dot{\gamma} = \dot{\gamma}^*$. (a) Influence of selected material parameters. (b) Influence of the strain at perturbation.

no effect on the ductility of the material in dynamic shearing. This issue will be further discussed in section 7.1 and Appendix B.

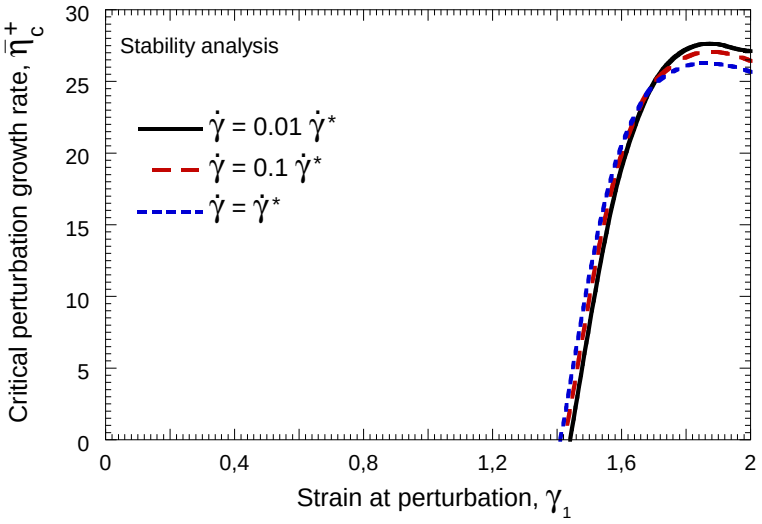

Figure 4: Stability analysis results. Critical perturbation growth rate $\bar{\eta}_c^+$ versus strain at perturbation γ_1 for different loading rates: $\dot{\gamma} = 0.01\dot{\gamma}^*$, $\dot{\gamma} = 0.1\dot{\gamma}^*$ and $\dot{\gamma} = \dot{\gamma}^*$ (reference loading rate).

Fig. 5 shows that the curve $\bar{\eta}^+ - \bar{\xi}$ is affected by the strain rate despite the critical perturbation growth rate $\bar{\eta}_c^+$ is not. In this graph we illustrate the perturbation growth rate $\bar{\eta}^+$ versus the wavenumber $\bar{\xi}$ for different loading rates: $\dot{\gamma} = 0.01\dot{\gamma}^*$, $\dot{\gamma} = 0.1\dot{\gamma}^*$ and $\dot{\gamma} = \dot{\gamma}^*$. The strain at perturbation is $\gamma_1 = 1.8$. The reference material parameters are taken, Table 1. It is observed that increasing $\dot{\gamma}$ has a damping effect on long wavelength modes. This leads to increasing values of the dominant wavenumber as the loading rate increases, although the critical perturbation growth rate remains largely constant.

6.2. Influence of strain rate sensitivity

Fig. 6 shows the critical perturbation growth rate $\bar{\eta}_c^+$ versus the strain at perturbation γ_1 for different values of the strain rate sensitivity exponent: $m = 0.25m^*$, $m = 0.5m^*$, $m = m^*$ (reference value) and $m = 2m^*$. We have that the loss of stability starts for $\gamma_1 \approx 1.4$, irrespective of the value of the strain rate sensitivity parameter. Then, the critical perturbation growth rate increases with γ_1, until it reaches a maximum for $\gamma_1 \approx 1.9$. Larger values of the strain at perturbation lead to a smooth decrease in $\bar{\eta}_c^+$. Moreover, we note

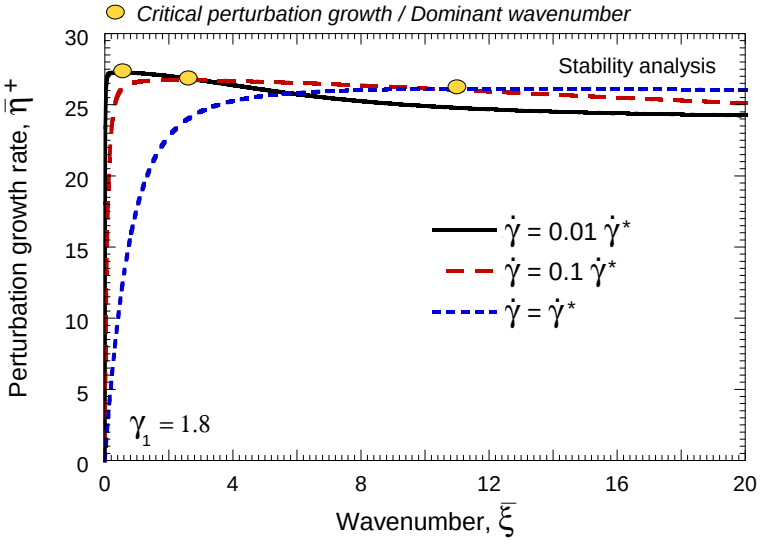

Figure 5: Stability analysis results. Perturbation growth rate $\bar{\eta}^+$ versus wavenumber $\bar{\xi}$ for different loading rates: $\dot{\gamma} = 0.01\dot{\gamma}^*$, $\dot{\gamma} = 0.1\dot{\gamma}^*$ and $\dot{\gamma} = \dot{\gamma}^*$ (reference loading rate). The strain at perturbation is $\gamma_1 = 1.8$.

that increasing m causes a large decrease in $\bar{\eta}_c^+$. In agreement with Molinari and Clifton (1987) and Molinari (1997), the viscosity is expected to stabilize the material behaviour and delay shear localization. This point will be further discussed in section 7.2.

6.3. Influence of thermal softening

Fig. 7 shows the critical perturbation growth rate $\bar{\eta}_c^+$ versus the strain at perturbation γ_1 for different values of the temperature sensitivity parameter: $\alpha = 0$, $\alpha = \alpha^*$ (reference value), $\alpha = 4\alpha^*$ and $\alpha = 8\alpha^*$. We observe that the value of α affects largely the $\bar{\eta}_c^+ - \gamma_1$ curves. Increasing thermal softening reduces the value of strain for which the material becomes unstable, and increases the perturbation growth rate. In other words, thermal softening boosts shear localization (Molinari and Clifton, 1987; Molinari, 1997). Note that, if we take $\alpha = 8\alpha^*$, the perturbation starts to grow before the material develops dynamic recrystallization (see Fig. 7). This is not the case if we take $\alpha = 4\alpha^*$, $\alpha = \alpha^*$ or $\alpha = 0$. For these temperature sensitivity parameters, instability is only attained once DRX starts to develop. This result illustrates the competition between these two destabilizing mechanics. On the one hand, dynamic recrystallization leads to strain softening which promotes localization. On the other hand, temperature sensitivity leads to thermal softening which

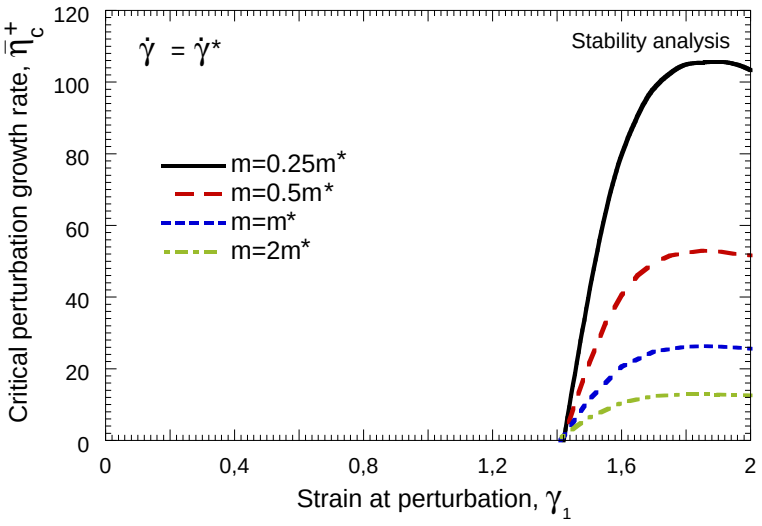

Figure 6: Stability analysis results. Critical perturbation growth rate $\bar{\eta}_c^+$ versus strain at perturbation γ_1 for different values of the strain rate sensitivity exponent: $m = 0.25m^*$, $m = 0.5m^*$, $m = m^*$ (reference value) and $m = 2m^*$. The reference loading rate $\dot{\gamma} = \dot{\gamma}^*$ is considered.

favours localization as well. Depending on their respective contribution, the dominant destabilizing mechanism responsible for the shear localization can alternate from one to the other. In any case, they are complementary factors which trigger localization. This key issue will be matter of discussion in forthcoming sections of the paper.

6.4. Influence of dynamic recrystallization

In Fig. 8 we illustrate the critical perturbation growth rate $\bar{\eta}_c^+$ versus the strain at perturbation γ_1 for different values of the threshold energy for DRX formation: $U_{DRX} = 0.125U^*$, $U_{DRX} = 0.25U^*$, $U_{DRX} = 0.5U^*$, $U_{DRX} = U^*$ (reference value) and $U_{DRX} = 1.25U^*$. We observe that decreasing the threshold energy for DRX formation causes a drastic reduction in the value of γ_1 at which the material becomes unstable and, at the same time, a large increase in the critical perturbation growth rate. It is therefore expected that materials prone to develop dynamic recrystallization will be subjected to early shear localization. This behaviour was pointed out by Rittel et al. (2006) and Osovski et al. (2012b) in a series of dynamic experiments recently published.

Altogether, the results presented in this section devoted to the linear stability analysis point to the following key issues:

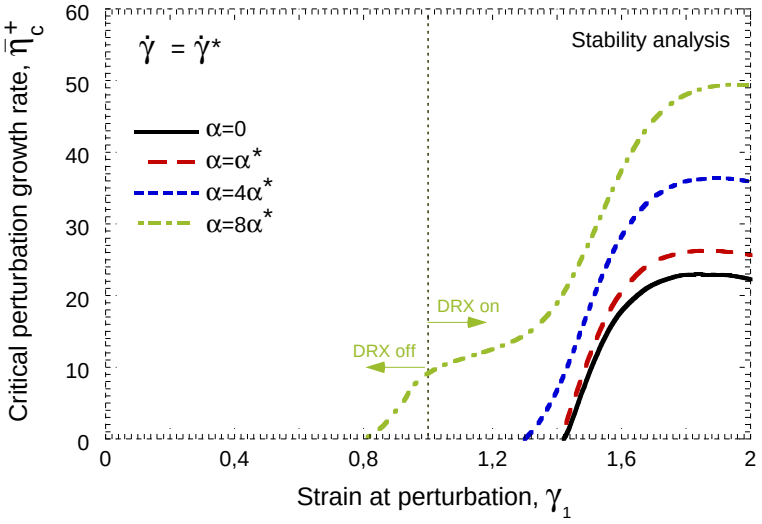

Figure 7: Stability analysis results. Critical perturbation growth rate $\bar{\eta}_c^+$ versus strain at perturbation γ_1 for different values of the temperature sensitivity parameter: $\alpha = 0$, $\alpha = \alpha^*$ (reference value), $\alpha = 4\alpha^*$ and $\alpha = 8\alpha^*$. The reference loading rate is taken $\dot{\gamma} = \dot{\gamma}^*$.

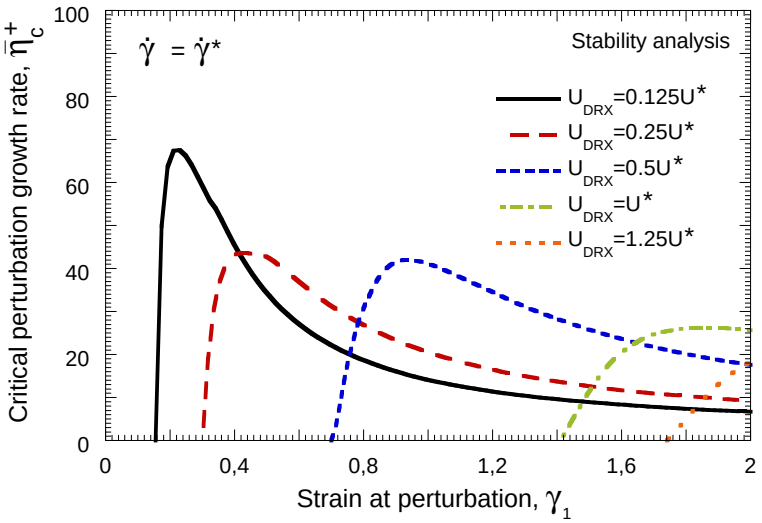

Figure 8: Stability analysis results. Critical perturbation growth rate $\bar{\eta}_c^+$ versus strain at perturbation γ_1 for different values of the threshold energy for DRX formation: $U_{DRX} = 0.125U^*$, $U_{DRX} = 0.25U^*$, $U_{DRX} = 0.5U^*$, $U_{DRX} = U^*$ (reference value) and $U_{DRX} = 1.25U^*$. The reference loading rate $\dot{\gamma} = \dot{\gamma}^*$ is considered.

- Strain rate barely affects the critical perturbation growth rate. This suggests a small (negligible) influence of the loading rate in the shear localization strain for the material analysed in this paper.

- Strain rate sensitivity substantially decreases the critical perturbation growth rate. It is expected that a material with large rate sensitivity shall experience delay and slowdown of shear localization.

- Thermal softening boosts the critical perturbation growth rate. Increasing material temperature sensitivity shall anticipate and speed up shear localization.

- Dynamic recrystallization enhances the critical perturbation growth rate. The perturbation analysis predicts that DRX development may have a role in triggering shear localization, competing with the thermal softening as the main responsible for the formation of shear bands.

Next, these key outcomes of the linear stability analysis are complemented with the finite element results.

7. Finite element results

We proceed according to the scheme developed in section 6, investigating sequentially the roles that strain rate (section 7.1), strain rate sensitivity (section 7.2), thermal softening (section 7.3) and dynamic recrystallization (section 7.4) all have in shear localization. As in previous section, unless otherwise noted, the reference material parameters listed in Table 1 are taken. The imperfection amplitude Δ^* is considered.

7.1. Influence of strain rate

Fig. 9 shows the average strain in side B ($\bar{\gamma}_B$) versus average strain in side A ($\bar{\gamma}_A$) for different loading rates: $\dot{\gamma} = 0.01\dot{\gamma}^*$, $\dot{\gamma} = 0.1\dot{\gamma}^*$, $\dot{\gamma} = 0.5\dot{\gamma}^*$, $\dot{\gamma} = \dot{\gamma}^*$ and $\dot{\gamma} = 2\dot{\gamma}^*$. For the comparison, the strains in sides A and B have been averaged over their corresponding lengths (L_A and L_B). This approach, which is regularly applied in the interpretation of experimental data, is required since for large deformations the strains along sides A and

B may not be fully uniform. On the other hand, the average strains can provide reliable measurements which are representative of the problem addressed. Following Molinari and Clifton (1987), the strain at which localization occurs, also called critical shear strain and denoted by γ_c, is taken as the strain for which the curve $\bar{\gamma}_B - \bar{\gamma}_A$ exhibits a vertical asymptote. In the sequel, the localization strain corresponding to the reference material parameters, loading rate and imperfection amplitude will be denoted by γ_c^*.

Fig. 9 reveals that the loading rate has a negligible influence on the $\bar{\gamma}_B - \bar{\gamma}_A$ curves. This is in full agreement with the predictions of the stability analysis, the critical localization strain γ_c does not depend on the applied strain rate (the critical perturbation growth rate hardly depends on the applied strain rate in Fig. 4). This behaviour is distinctive of the specific material description considered here since, in the general case, the strain rate leads to material stabilization as reported by Molinari (1985) and further shown in Appendix B.

Moreover, we note that the experimental results reported by several authors (see for example the works by Klepaczko (1998, 2005)) reveal a drastic decrease in shear ductility once a threshold in applied velocity is exceeded (of the order of several tens of meters per second in mild steels). This drop in the shear failure strain of the material is defined by Klepaczko (1998, 2005) as the Critical Impact Velocity (CIV). Localization of plastic deformation in adiabatic conditions superimposed to wave effects decrease the plastic wave speed until it reaches zero and the CIV occurs (Klepaczko, 2005). In our numerical calculations, we initialize the velocity and stress fields to be in agreement with the initial conditions applied in the stability analysis (see section 4). This procedure precludes waves disturbances and therefore attainment of the critical impact velocity. It can be noted that the CIV and the corresponding drop in ductility are structural (wave related) effects, whereas the constant (strain rate independent) ductility shown in Fig. 9 is a material (constitutive) effect.

Fig. 9 also shows that at low strains the plastic flow is (quasi)homogeneous in the sample and that $\bar{\gamma}_B \approx \bar{\gamma}_A$. The (quasi)homogeneous state of stresses and strains is maintained until $\bar{\gamma}_A \sim 0.41$. Larger values of $\bar{\gamma}_A$ lead to the a *stable* heterogeneity in the strains field. Larger strains are found in side B than in side A, but the plastic flow is not yet fully localized. Complete localization occurs for $\bar{\gamma}_A \sim 0.72$. Then, the strains on side A do not further

increase and the plastic flow concentrates in a narrow band close to side B. This can be referred to as *full* or *strong* localization.

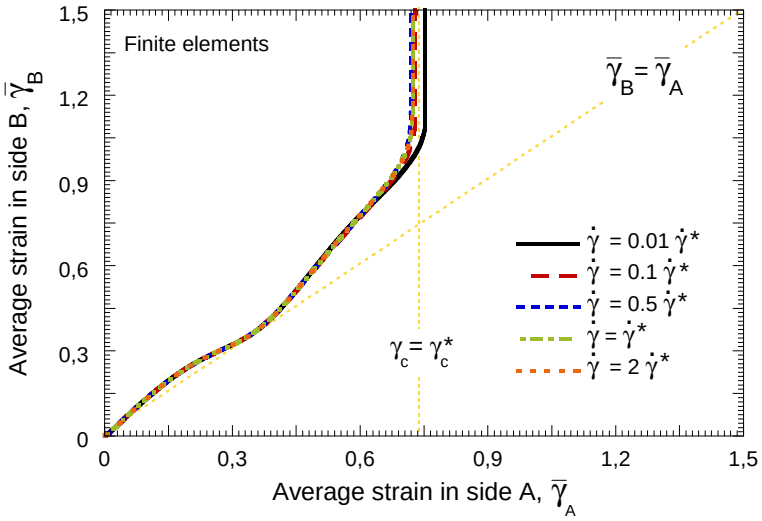

Figure 9: Finite element results. Average strain in side B ($\bar{\gamma}_B$) versus average strain in side A ($\bar{\gamma}_A$) for different loading rates: $\dot{\gamma} = 0.01\dot{\gamma}^*$, $\dot{\gamma} = 0.1\dot{\gamma}^*$, $\dot{\gamma} = 0.5\dot{\gamma}^*$, $\dot{\gamma} = \dot{\gamma}^*$ and $\dot{\gamma} = 2\dot{\gamma}^*$.

These different *steps* that were identified during the loading process are illustrated in Fig. 10, where contours of equivalent plastic strain $\bar{\varepsilon}^p$ for different loading times are shown. In Fig. 10(a) we have $\bar{\gamma}_A = 0.27$ which (see Fig. 9) corresponds to a (quasi)homogeneous strain field. Fig. 10(b) corresponds to $\bar{\gamma}_A = 0.51$ for which the strain field shows an *stable* heterogeneity (see Fig. 9). The onset of localization is illustrated in Fig. 10(c) where one can observe the incipient formation of a shear band on side B. Fig. 10(d) corresponds to $\bar{\gamma}_A = 0.72$ and the plastic strain is already fully localized leading to the propagation of the shear band along side B. Within the localized region, we find temperatures ranging between 450 K and 600 K. The computations predict a finite width of the shear band which is, to a large extent, controlled by the element size (see Zukas and Scheffer (2000)). It is not within the goals of this work to discuss the influence of the mesh on the width of shear bands calculated by the finite element method. This issue has been carefully analysed for example by Bonnet-Lebouvier et al. (2002). In this paper we are exclusively interested in the initiation of the shear band, and more specifically by the strain which corresponds to its initiation. After carrying out a mesh convergence analysis (details are given in Appendix A), this value of strain γ_c has been found to be largely independent of

the discretization.

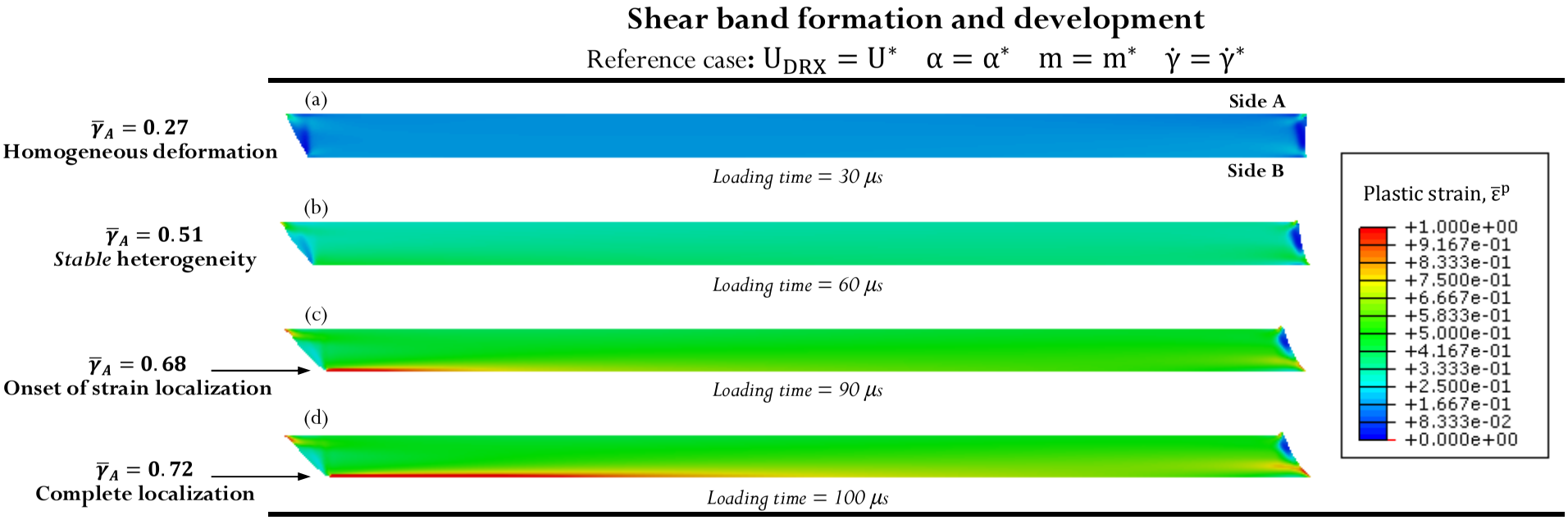

Figure 10: Finite element results. The reference loading rate is taken $\dot{\gamma} = \dot{\gamma}^*$. Contours of equivalent plastic strain ($\bar{\varepsilon^p}$) for different loading times: (a) Loading time = 30 μs, $\bar{\gamma}_A = 0.27$, (b) Loading time = 60 μs, $\bar{\gamma}_A = 0.51$, (c) Loading time = 90 μs, $\bar{\gamma}_A = 0.68$, (e) Loading time = 100 μs, $\bar{\gamma}_A = 0.72$.

7.2. Influence of strain rate sensitivity

The average strain in side B ($\bar{\gamma}_B$) versus average strain in side A ($\bar{\gamma}_A$) is shown in Fig. 11 for different values of the strain rate sensitivity exponent: $m = 0.25m^*$, $m = 0.5m^*$, $m = m^*$ and $m = 2m^*$. During the stage of (quasi)homogeneous deformation the curve $\bar{\gamma}_B - \bar{\gamma}_A$ is not affected by the strain rate sensitivity. This ceases at the onset of the phase of *stable* heterogeneity, when the curves shown in Fig. 11 are no longer superimposed. The heterogeneity in the strains field is more noticeable as the rate sensitivity exponent decreases, i.e. the gradient of strain from side A to B is more pronounced as m decreases. Consequently, decreasing material rate sensitivity favours shear localization.

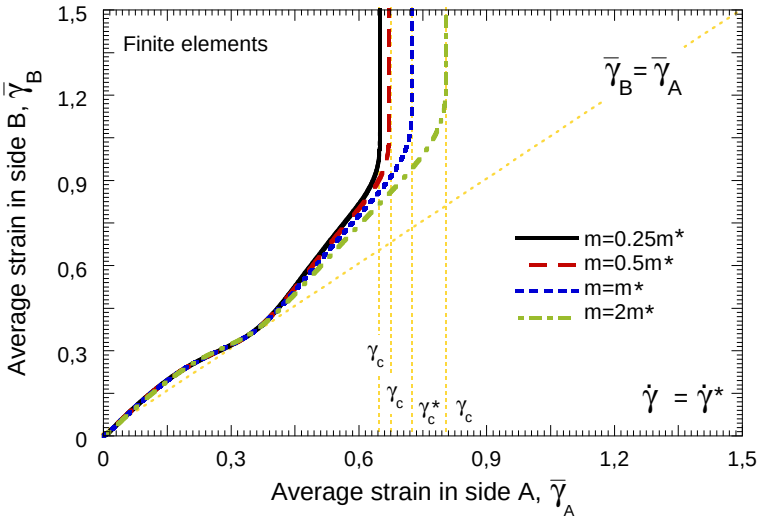

Figure 11: Finite element results. Average strain in side B ($\bar{\gamma}_B$) versus average strain in side A ($\bar{\gamma}_A$) for different values of the strain rate sensitivity exponent: $m = 0.25m^*$, $m = 0.5m^*$, $m = m^*$ (reference value) and $m = 2m^*$. The reference loading rate $\dot{\gamma} = \dot{\gamma}^*$ is considered.

This behaviour is further illustrated in Fig. 12 showing the normalized critical shear strain γ_c/γ_c^* versus the normalized strain rate sensitivity exponent m/m^*. The stabilizing effect of strain rate sensitivity which leads to a substantial increase in γ_c/γ_c^* with m/m^* is noticeable. Namely, going from $\gamma_c/\gamma_c^* \approx 0.89$ in the case of $m/m^* = 0.25$, to $\gamma_c/\gamma_c^* \approx 1.17$ in the case of $m/m^* = 2$. The stabilizing role of strain rate sensitivity revealed by the computations is in excellent agreement with the results of the perturbation analysis showing a decrease in the critical perturbation growth rate as the material rate sensitivity increases (Fig. 6).

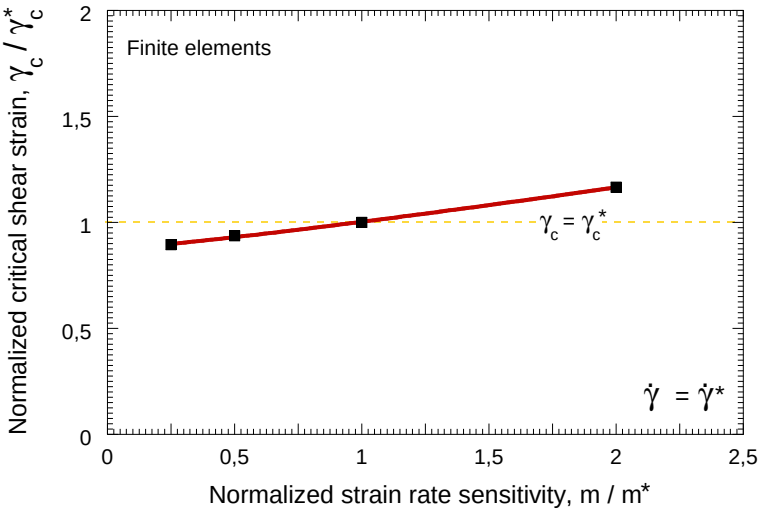

Figure 12: Finite element results. Normalized critical shear strain γ_c/γ_c^* versus normalized strain rate sensitivity exponent m/m^*. The reference loading rate $\dot{\gamma} = \dot{\gamma}^*$ is considered.

7.3. Influence of thermal softening

The average strain in side B ($\bar{\gamma}_B$) versus average strain in side A ($\bar{\gamma}_A$) is shown in Fig. 13 for different values of the temperature sensitivity parameter: $\alpha = 0$, $\alpha = \alpha^*$ (reference value), $\alpha = 4\alpha^*$ and $\alpha = 8\alpha^*$.

All the $\bar{\gamma}_B - \bar{\gamma}_A$ curves lie together during the process of (quasi)homogeneous deformation. Thermal softening plays a role during the stage of stable heterogeneity. It is shown that increasing the temperature sensitivity parameter promotes shear localization. On the other hand, it has to be noted that thermal effects are not indispensable to attain localization. In the limiting case where $\alpha = 0$, the calculation still predicts the inception of the shear band. In the absence of thermal softening, the source of material destabilization is the strain softening caused by dynamic recrystallization. Setting $\alpha = 0$ provides an idea about the major role that development of DRX may have in the shear localization. There results are consistent with the results extracted from the stability analysis. We showed in Fig. 7 the destabilizing role of the thermal effects represented by the increase of the critical perturbation growth rate as we increased α. Likewise, in the same graph it was shown that the material may reach instability in absence of thermal effects.

Fig. 14 shows the normalized critical shear strain γ_c/γ_c^* versus the normalized temperature sensitivity parameter α/α^*. A non-linear concave-up decrease in γ_c/γ_c^* corresponds

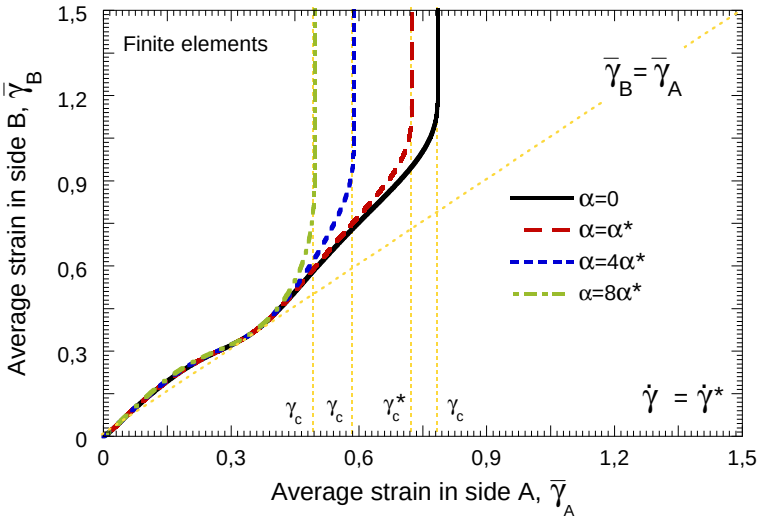

Figure 13: Finite element results. Average strain in side B ($\bar{\gamma}_B$) versus average strain in side A ($\bar{\gamma}_A$) for different values of the temperature sensitivity parameter: $\alpha = 0$, $\alpha = \alpha^*$ (reference value), $\alpha = 4\alpha^*$ and $\alpha = 8\alpha^*$. The loading rate is $\dot{\gamma} = \dot{\gamma}^*$.

to an increase in the normalized temperature sensitivity of the material α/α^*. Namely, $\gamma_c/\gamma_c^* \approx 1.08$ for the athermal material and $\gamma_c/\gamma_c^* \approx 0.69$ in the case of $\alpha/\alpha^* = 8$.

Taking into account the results of our previous work (Rodríguez-Martínez et al., 2014), it seems that thermal softening plays a more determinant role in the inception of shear bands than in the formation of necks. This may be because, unlike necking, the shear bands can be considered as material instabilities, therefore requiring the operation of a softening mechanism. These softening mechanisms, whether of a thermal or microstructural nature (DRX, see section 7.4), are the main mechanisms that control shear band formation.

7.4. Influence of dynamic recrystallization

Fig. 15 illustrates the average strain in side B ($\bar{\gamma}_B$) versus average strain in side A ($\bar{\gamma}_A$) for different values of the threshold energy for DRX formation: $U_{DRX} = 0.125U^*$, $U_{DRX} = 0.25U^*$, $U_{DRX} = 0.5U^*$, $U_{DRX} = U^*$ and $U_{DRX} = 1.25U^*$.

The $\bar{\gamma}_B - \bar{\gamma}_A$ curves obtained for the different values of U_{DRX} investigated only lie together during the very first stages of the loading process. The curve corresponding to $U_{DRX} = 0.125U^*$ (this is the smallest threshold energy for dynamic recrystallization that we have considered) deviates very soon from the condition $\bar{\gamma}_A = \bar{\gamma}_B$, developing full

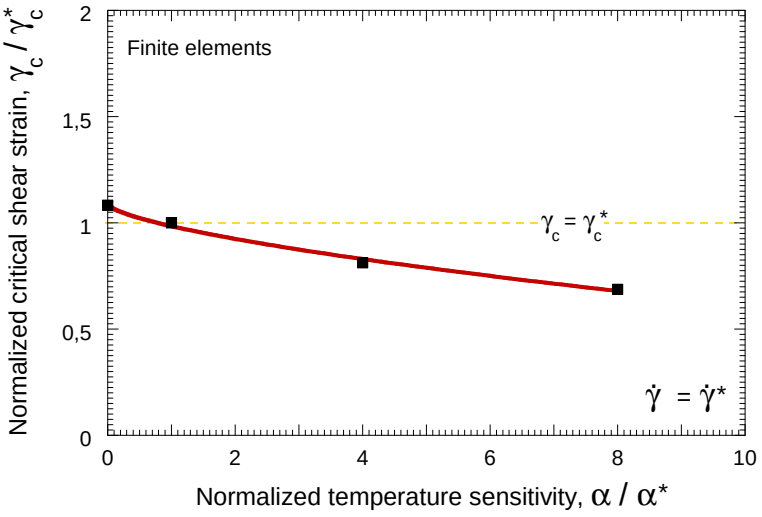

Figure 14: Finite element results. Normalized critical shear strain γ_c/γ_c^* versus normalized temperature sensitivity parameter α/α^*. The reference loading rate $\dot{\gamma} = \dot{\gamma}^*$ is considered.

localization for $\gamma_c \approx 0.15$. Similar behaviour is observed in the case of $U_{DRX} = 0.25U^*$ (this is the second smallest value considered) for which complete localization occurs at $\gamma_c \approx 0.30$. To be noted that for these two values of U_{DRX} the sample passes directly from the loading stage named before as (quasi)homogeneous (the curve lies in the condition $\bar{\gamma}_A = \bar{\gamma}_B$) to the full localization stage (the curve $\bar{\gamma}_B - \bar{\gamma}_A$ finds a vertical asymptote). It does not undergo the loading stage referred to as stable heterogeneity in previous sections of the paper (stable deviation from the $\bar{\gamma}_A = \bar{\gamma}_B$ condition). This stage only appears with increasing values of U_{DRX}, which delay the shear band inception. For $U_{DRX} = 0.5U^*$, $U_{DRX} = U^*$ and $U_{DRX} = 1.25U^*$ we observe late flow localization. In these cases, the sample firstly undergoes the phase of (quasi)homogeneous deformation, followed by the stage of stable heterogeneity and, ultimately, by the inception the shear band.

Fig. 16 shows contours of volume fraction of DRX (f_{DRX}) for different values of the threshold energy for DRX formation: (a) $U_{DRX} = 0.125U^*$, (b) $U_{DRX} = 0.25U^*$, (c) $U_{DRX} = 0.5U^*$, (d) $U_{DRX} = U^*$ (reference value) and (d) $U_{DRX} = 1.25U^*$. In each case the loading time corresponds to the time of full localization. In the cases of $U_{DRX} = 0.125U^*$ and $U_{DRX} = 0.25U^*$ dynamic recrystallization has developed in the specimen which favours early plastic localization. By contrast, if we consider $U_{DRX} = 0.5U^*$, $U_{DRX} = U^*$ or $U_{DRX} = 1.25U^*$ dynamic recrystallization is only detected in a narrow band close to side

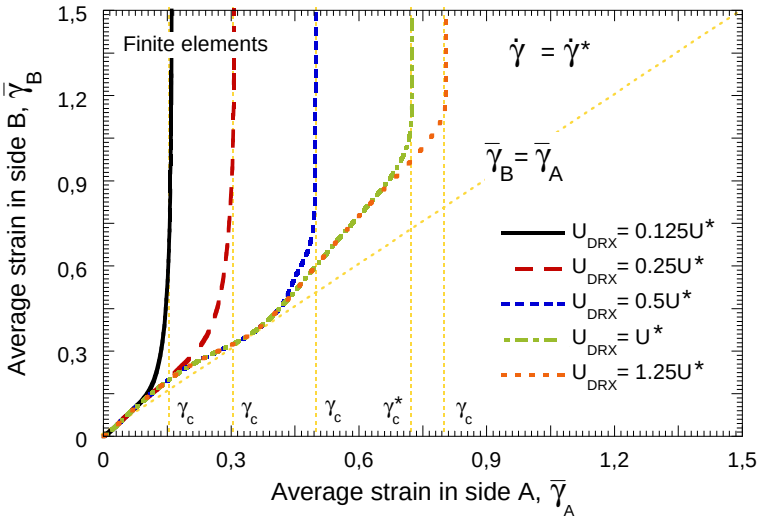

Figure 15: Finite element results. Average strain in side B ($\bar{\gamma}_B$) versus average strain in side A ($\bar{\gamma}_A$) for different values of the threshold energy for DRX formation: $U_{DRX} = 0.125U^*$, $U_{DRX} = 0.25U^*$, $U_{DRX} = 0.5U^*$, $U_{DRX} = U^*$ (reference value) and $U_{DRX} = 1.25U^*$. The reference loading rate $\dot{\gamma} = \dot{\gamma}^*$ is taken.

B, in the plane where the shear band is incepted.

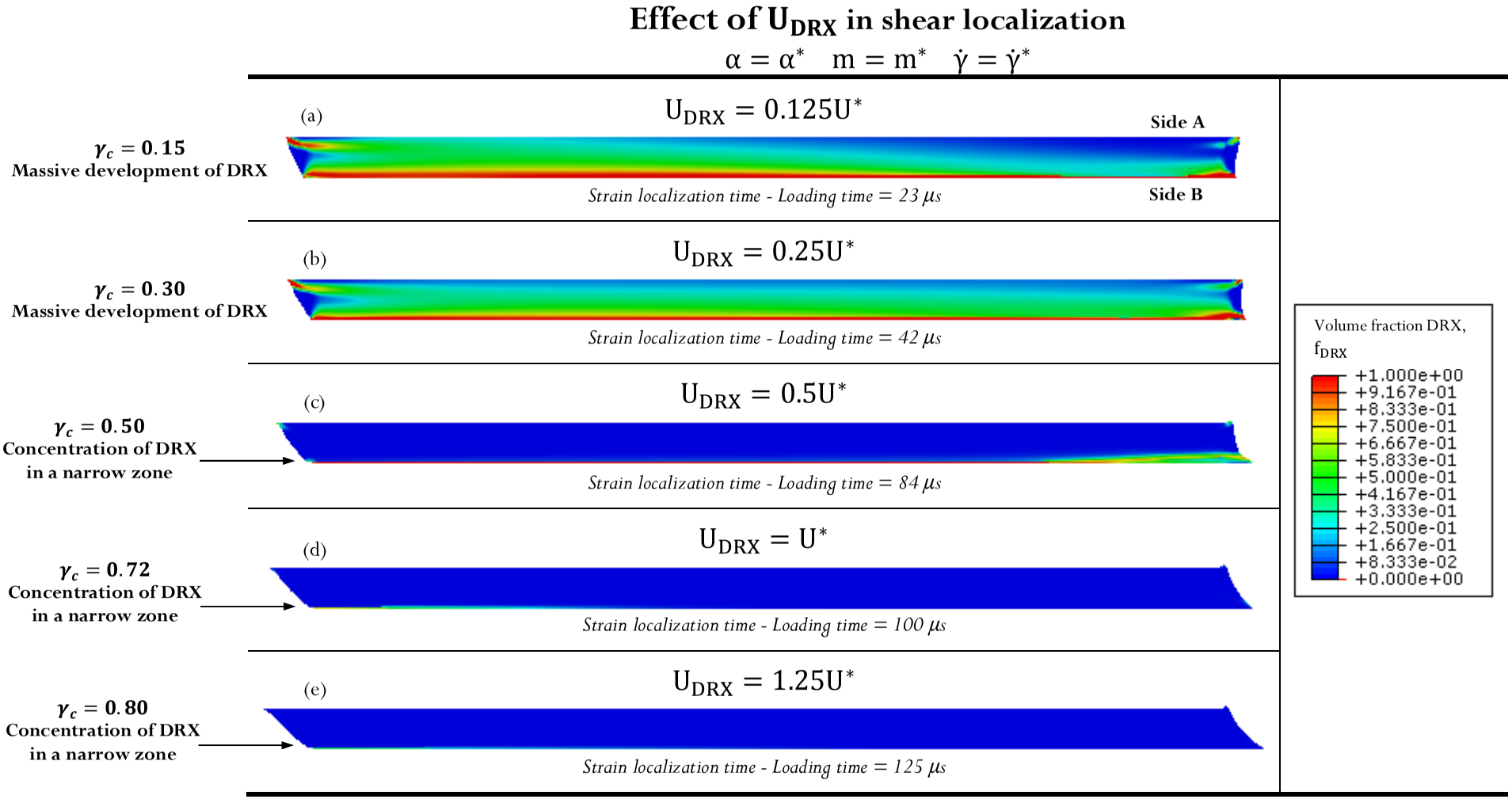

Figure 16: Finite element results. The reference loading rate is taken $\dot{\gamma} = \dot{\gamma}^*$. Contours of volume fraction of DRX (f_{DRX}) for different values of the for different values of the threshold energy for DRX formation: (a) $U_{DRX} = 0.125U^*$, (b) $U_{DRX} = 0.25U^*$, (c) $U_{DRX} = 0.5U^*$, (d) $U_{DRX} = U^*$ (reference value) and (d) $U_{DRX} = 1.25U^*$. In each case the loading time corresponds to the time of shear localization.

Altogether, the numerical computations reveal the strong destabilizing role played by the dynamic recrystallization. This is further illustrated in Fig. 17 where the normalized critical shear strain γ_c/γ_c^* versus the normalized threshold energy for DRX formation U_{DRX}/U^* is shown. A non-linear concave-down increase in γ_c/γ_c^* with U_{DRX}/U^* is reported. Namely, going from $\gamma_c/\gamma_c^* \approx 0.21$ for $U_{DRX}/0.125U^*$ to $\gamma_c/\gamma_c^* \approx 1.1$ for $U_{DRX}/1.25U^*$. Note that lowering the ratio U_{DRX}/U^* below ~ 0.5 causes a dramatic decrease in the strain corresponding to the shear band inception. These observations are in perfect agreement with the results obtained from the stability analysis (see Fig. 8) which showed a strong increase of the critical perturbation growth rate, specially for the smaller ratios of U_{DRX}/U^* investigated (the black curve in Fig. 8 stands above the rest).

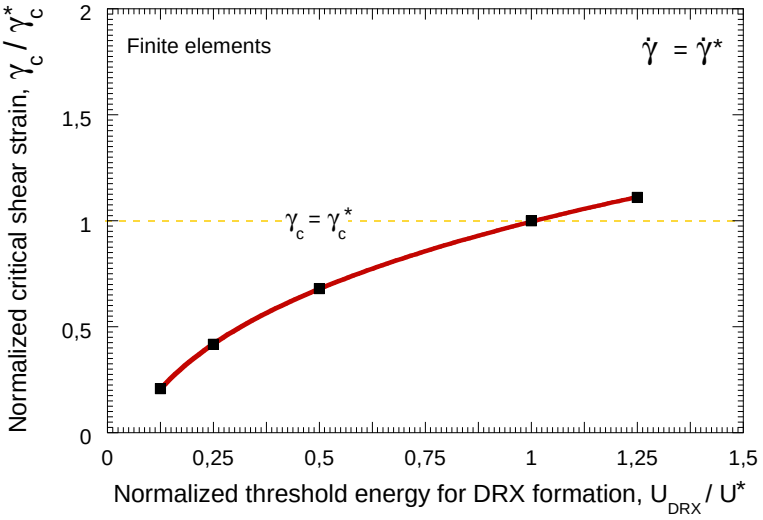

Figure 17: Finite element results. Normalized critical shear strain γ_c/γ_c^* versus normalized threshold energy for DRX formation U_{DRX}/U^*. The reference loading rate $\dot{\gamma} = \dot{\gamma}^*$ is considered.

Overall, the results elaborated from the numerical computations corroborate the predictions obtained from the linear perturbation analysis:

- It is confirmed that, in absence of waves disturbances, the loading rate barely affects the shear ductility for the material investigated in this paper.
- It is ratified the stabilizing role played by the strain rate sensitivity which homogenizes the field of strains in the sample and delays shear band inception.

- On the one hand it is clearly shown that thermal softening favours the inception of the shear band. On the other hand it is shown that flow localization can be triggered in absence of thermal effects whenever another softening mechanism as dynamic recrystallization is present.

- The results show the strong destabilizing effect played by the development of dynamic recrystallization, that seems to be the main responsible for shear localization in materials showing this type of microstructural evolution.

8. Discussion and conclusions

In this work, we have presented an analysis of the inception of dynamic shear instabilities (adiabatic shear bands) for a shear-loaded solid. Two approaches were used here, namely a 1D analytical study and a 2D numerical one. This research lies within the theoretical framework developed in the works of Molinari and Clifton (1987) and Molinari (1997), in which the growth of small perturbations is used to investigate the stability of the material. It should also be noted that the methodology developed here follows the approach used in our recent work on dynamic necking instability (Rodríguez-Martínez et al., 2014), adapted to the specific shear problem at hand. However, while the latter was not supported by experimental evidence, the present work is fully motivated by the experimental observations of Osovski and Rittel (2012) and Osovski et al. (2012a,b). In other words, the general stability issue under dynamic shear was studied, with the new aspect of including a potent destabilizing factor, namely microstructural evolutions, i.e. dynamic recrystallization, as observed by Osovski et al. (2013). From a purely mechanical standpoint, microstructural evolutions can be regarded as one more destabilizing factor, so that one would expect it to complement the effects of the well-considered thermal softening. However, from a physical standpoint, it should be emphasized that microstructural softening is, in itself, a sufficiently central factor so that it can destabilize the material behavior, without the need to resort to thermal softening. It can therefore be said that the current work extends in a sense the previous classical analyses of dynamic shear localization of Molinari and Clifton (1987) and Molinari (1997), together with the addition of a numerical part and the consideration of additional destabilizing factors related to the microstructure.

The extension consists, therefore, in the fact that the full set of relevant physical factors is now examined and allowed to compete regarding the onset of the dynamic shear instability, whereas until now, thermal softening was the sole factor that was investigated. A first observation is that the numerical results which are closer to experimental reality, albeit not including wave propagation effects, are fully compatible with the simplified 1D analytical approach. Another important result, which fully matches the experimental observations (Osovski and Rittel, 2012; Osovski et al., 2012a), is that microstructural softening is, in itself, sufficient to trigger the dynamic shear instability formation. As expected, strain-rate sensitivity plays a stabilizing role in the studied problem. Altogether, the results of the present study, dedicated to shear, bear a definite resemblance to those obtained for the dynamic tensile instability. As such, not only does the present study, motivated by physical observations, extend previous analytical studies, but it can be concluded that by its similarity to the necking problem, it confers a wider generality to the generic problem of mechanical instabilities in dynamically strained solids.

Thus, the following general conclusions can be drawn from the present study:

- The stability analysis regarding the onset of shear instabilities is extended by considering microstructural-related softening.
- When microstructural effect is taken into account in addition to thermal softening, it is found that the former is a potent destabilizing effect in itself, in full accord with previous experimental evidence.
- The results of the present stability analysis, which addresses shear, show a definite resemblance to those of the dynamic necking problem.
- As such, the present analysis complements and adds generality to the generic problem of dynamic mechanical instabilities in strained solids.

Acknowledgements

The authors are indebted to the *Ministerio de Ciencia e Innovación de España* (Projects DPI/2011-24068 and DPI/2011-23191) for the financial support.

The authors express sincere gratitude to Professor Alain Molinari for helpful discussions in strain localization problems. His contributions to the field of dynamic shear localization have been a main source of inspiration for this work.

Appendix A. Numerical sensitivity analysis

Fig. A.18 shows the normalized critical shear strain γ_c/γ_c^* versus the normalized imperfection amplitude Δ/Δ^*. The threshold energy for DRX formation is $U_{DRX} = 0.25U^*$. The strong effect played by the imperfection amplitude in the shear localization strain is observed. A non-linear concave-up decrease in γ_c/γ_c^* with Δ/Δ^* is reported. Ultimately we have that $\gamma_c/\gamma_c^* \to \infty$ if $\Delta/\Delta^* \to 0$ and $\gamma_c/\gamma_c^* \to 0$ if $\Delta/\Delta^* \to \infty$. In this regard, we have to note that Molinari and Clifton (1987) already reported similar results obtained from numerical simulations of the shear localization problem.

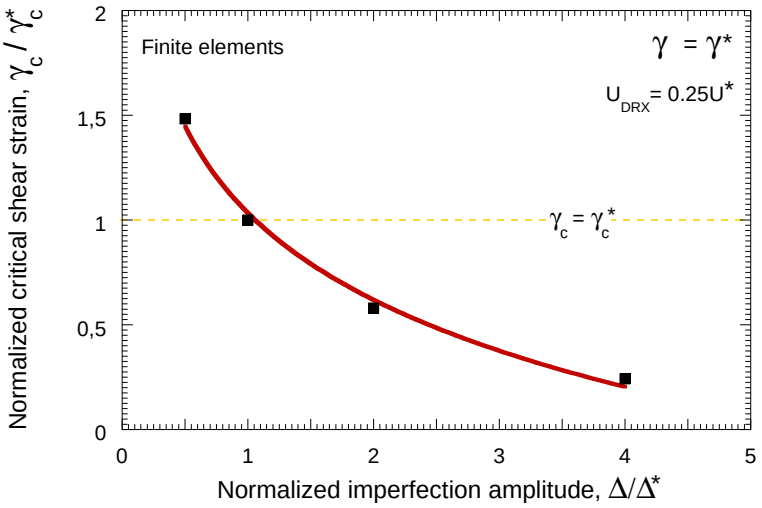

Figure A.18: Finite element results. Normalized critical shear strain γ_c/γ_c^* versus normalized imperfection amplitude Δ/Δ^*. The threshold energy for DRX formation is $U_{DRX} = 0.25U^*$. The reference loading rate $\dot{\gamma} = \dot{\gamma}^*$ is considered.

Fig. A.19 shows the average strain in side B ($\bar{\gamma}_B$) versus the average strain in side A ($\bar{\gamma}_A$) for different mesh densities: 20×470 elements, 30×705 elements and 40×940 elements. The threshold energy for DRX formation is $U_{DRX} = 0.25U^*$. We observe the overlapping of the $\bar{\gamma}_B - \bar{\gamma}_A$ curves obtained for the three meshes investigated in Fig. A.19. The differences in the critical shear strain are negligible. Therefore, in order to have the smallest possible

computational time, the coarser mesh was used in all the numerical simulations shown in this paper.

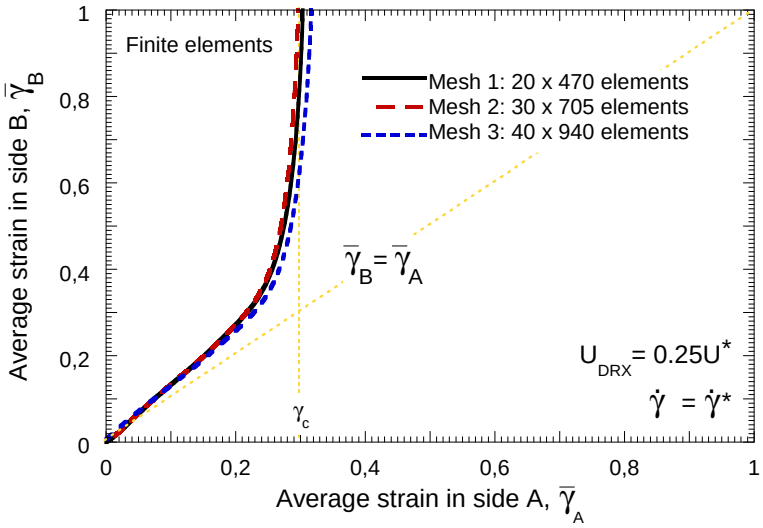

Figure A.19: Finite element results. Average strain in side B ($\bar{\gamma}_B$) versus average strain in side A ($\bar{\gamma}_A$) for different mesh densities: 20×470 elements (reference mesh), 30×705 elements and 40×940 elements. The threshold energy for DRX formation is $U_{DRX} = 0.25U^*$. The loading rate is $\dot{\gamma} = \dot{\gamma}^*$.

Appendix B. Inertia sensitivity analysis

In order to investigate the effect that, exclusively inertia (via strain rate), has on the critical shear strain we rely on the elastic perfectly-plastic material such that $\tau_y = 288.67\ MPa$. Isothermal conditions are considered. Fig. B.20 shows the average strain in side B ($\bar{\gamma}_B$) versus the average strain in side A ($\bar{\gamma}_A$) for different loading rates: $\dot{\gamma} = 0.01\dot{\gamma}^*$, $\dot{\gamma} = 0.1\dot{\gamma}^*$, $\dot{\gamma} = 0.5\dot{\gamma}^*$ and $\dot{\gamma} = \dot{\gamma}^*$. The absence of strain hardening, strain rate hardening and temperature softening in the material constitutive equations necessarily implies that the increasing value of the critical shear strain with loading rate is due to inertia effects (strain rate). The intrinsic effect of loading rate is to delay shear band formation as shown by Molinari (1985). The results shown in section 6.1 where the value of γ_c was largely independent of the strain rate applied are specific of the material behaviour there considered. In that case the stabilizing effect of inertia seems to be balanced by the destabilizing effects of temperature and DRX formation, which are favoured as the loading rate increases.

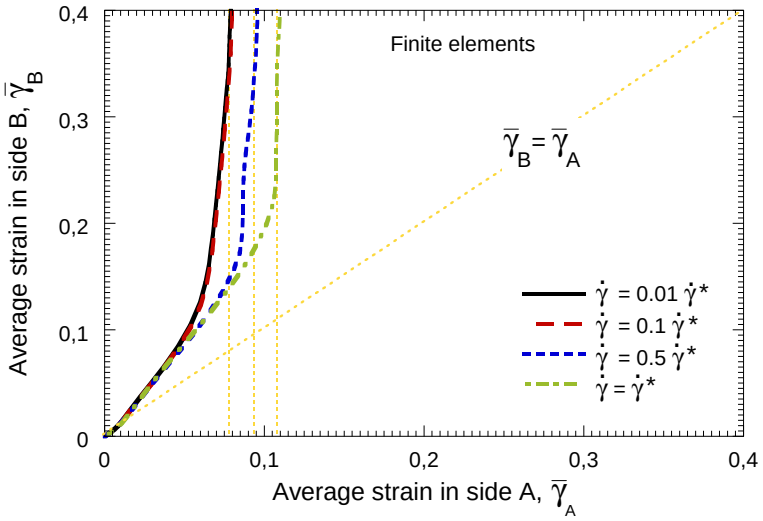

Figure B.20: Finite element results. Average strain in side B ($\bar{\gamma}_B$) versus the average strain in side A ($\bar{\gamma}_A$) for different loading rates: $\dot{\gamma} = 0.01\dot{\gamma}^*$, $\dot{\gamma} = 0.1\dot{\gamma}^*$, $\dot{\gamma} = 0.5\dot{\gamma}^*$ and $\dot{\gamma} = \dot{\gamma}^*$. The material yield stress is $\tau_y = 288.67\ MPa$.

References

Bai, Y., Dodd, B., 2012. Adiabatic Shear Localization, 2nd Edition. Elsevier.

Bonnet-Lebouvier, A. S., Molinari, A., Lipinski, P., 2002. Analysis of the dynamic propagation of adiabatic shear bands. International Journal of Solids and Structures 39, 4249–4269.

Dorogoy, A., Rittel, D., 2005. Numerical validation of the shear compression specimen. part II: Dynamic large strain testing. Experimental Mechanics 45, 178–185.

Dorogoy, A., Rittel, D., 2006. A numerical study of the applicability of the shear compression specimen to parabolic hardening materials. Experimental Mechanics 46, 355–366.

Klepaczko, J. R., 1998. Remarks on impact shearing. Journal of the Mechanics and Physics of Solids 46, 1028–1042.

Klepaczko, J. R., 2005. Review on critical impact velocities in tension and shear. International Journal of Impact Engineering 32, 188–209.

Lovinger, Z., Rikanati, A., Rosenberg, Z., Rittel, D., 2011. Electro-magnetic collapse of thick-walled cylinders to investigate spontaneous shear localization. International Journal of Impact Engineering 38, 918–929.

Marchand, A., Duffy, J., 1998. An experimental study of the formation process of adiabatic shear bands in a structural steel. Journal of the Mechanics and Physics of Solids 36, 251–283.

Molinari, A., 1985. Instabilité thermoviscoplastique en cisaillement simple. Journal de Mécanique Théorique et Appliquée 4, 659–684.

Molinari, A., 1997. Collective behaviour and spacing of adiabatic shear bands. Journal of the Mechanics and Physics of Solids 45, 1551–1575.

Molinari, A., Clifton, R. J., 1987. Analytical characterization of the shear localization in thermoviscoplastic materials. Journal of Applied Mechanics 54, 806–812.

Needleman, A., 1991. The effect of material inertia on neck development. In: Yang, W.H. (Ed.), Topics in Plasticity. AM Press, Ann Arbor, MI, 151–160.

Nesterenko, V. F., Bondar, M. P., 1994. Localization of deformation in collapse of a thick walled cylinder. Combustion, Explosion and Shock Waves 30, 500–505.

Nesterenko, V. F., Lazaridi, A. N., Pershin, S. A., 1989. Localization of deformation in copper by explosive compression of hollow cylinders. Fizika Goreniya i Vzryva 25, 154–155 (in Russian).

Osovski, S., Nahmany, Y., Rittel, D., Landau, P., Venkert, A., 2012a. On the dynamic character of localized failure. Scripta Materialia 67, 693–695.

Osovski, S., Rittel, D., 2012. Microstructural heterogeneity and dynamic shear localization. Applied Physics Letters 101, 211901.

Osovski, S., Rittel, D., Landau, P., Venkert, A., 2012b. Microstructural effects on adiabatic shear band formation. Scripta Materialia 66, 9–12.

Osovski, S., Rittel, D., Venkert, A., 2013. The respective influence of microstructural and thermal softening on adiabatic shear localization. Mechanics of Materials 56, 11–22.

Rittel, D., Landau, P., Venkert, A., 2008. Dynamic recrystallization as a potential cause for adiabatic shear failure. Physical Review Letters 101, 165501.

Rittel, D., Lee, S., Ravichandran, G., 2002a. A shear-compression specimen for large strain testing. Experimental Mechanics 42, 58–64.

Rittel, D., Ravichandran, G., Lee, S., 2002b. Large strain constitutive behavior of ofhc copper over a wide range strain rates using shear compression specimen. Mechanics of Materials 34, 627–642.

Rittel, D., Ravichandran, G., Venkert, A., 2006. The mechanical response of pure iron at high strain rates under dominant shear. Materials Science and Engineering A 432, 191–201.

Rodríguez-Martínez, J. A., Vadillo, G., Zaera, R., Fernández-Sáez, J., 2013. On the complete extinction of selected imperfection wavelengths in dynamically expanded ductile rings. Mechanics of Materials 60, 107–120.

Rodríguez-Martínez, J. A., Vadillo, G., Zaera, R., Fernández-Sáez, J., Rittel, D., 2014. An analysis of microstructural and thermal softening effects in dynamic necking. Mechanics of Materials, In press.

Simulia, 2012. ABAQUS/Explicit User's Manual, version 6.12 Edition. Dassault Systèmes, Providence, USA.

Vadillo, G., Rodríguez-Martínez, J. A., Fernández-Sáez, J., 2012. On the interplay between strain rate and strain rate sensitivity on flow localization in the dynamic expansion of ductile rings. International Journal of Solids and Structures 49, 481–491.

Vural, M., Molinari, A., Bhattacharyya, N., 2011. Analysis of slot orientation in shear-compression specimen (SCS). Experimental Mechanics 51, 263–273.

Wright, T. W., 2002. The Physics and Mathematics of Adiabatic Shear Bands, 1st Edition. Cambridge Monographs on Mechanics.

Xue, Z., Vaziri, A., Hutchinson, J. W., 2008. Material aspects of dynamic neck retardation. Journal of the Mechanics and Physics of Solids 56, 93–113.

Zaera, R., Fernández-Sáez, J., 2006. An implicit consistent algorithm for the integration of thermoviscoplastic constitutive equations in adiabatic conditions and finite deformations. International Journal of Solids and Structures 43, 1594–1612.

Zaera, R., Rodríguez-Martínez, J. A., Rittel, D., 2013. On the Taylor-Quinney coefficient in dynamically phase transforming materials. Application to 304 stainless steel. International Journal of Plasticity 40, 185–201.

Zaera, R., Rodríguez-Martínez, J. A., Vadillo, G., Fernández-Sáez, J., 2014. Dynamic necking in materials with strain induced martensitic transformation. Journal of the Mechanics and Physics of Solids 64, 316–337.

Zener, C., Hollomon, J. H., 1944. Effect of strain rate upon plastic flow of steel. Journal of Applied Physics 15, 22.

Zukas, J. A., Scheffer, D. R., 2000. Practical aspects of numerical simulations of dynamic events: effects of meshing. International Journal of Impact Engineering 24, 925–945.